

Simulating Solar Neighborhood Brown Dwarfs I: The Luminosity Function Above and Below the Galactic Plane

EASTON J. HONAKER¹ AND JOHN E. GIZIS¹

¹*Department of Physics and Astronomy, University of Delaware, Newark, DE 19716, USA*

ABSTRACT

Brown dwarfs form the key, yet poorly understood, link between stellar and planetary astrophysics. These objects offer unique tests of Galactic structure, but observational limitations have inhibited the large-scale analysis of these objects to date. Major upcoming sky surveys will reveal unprecedented numbers of brown dwarfs, among even greater numbers of stellar objects, enabling the statistical study of brown dwarfs. To extract the comparatively rare brown dwarfs from these massive datasets, we must understand how they will look in upcoming surveys. In this work, we construct a synthetic population of brown dwarfs in the Solar Neighborhood to explore their evolutionary properties using Gaia-derived star formation histories alongside observational mass, metallicity, and age relationships. We apply the cloudless Sonora Bobcat, hybrid SM08, and gravity-dependent hybrid Sonora Diamondback evolutionary models to the sample. We present the simulated luminosity function and its evolution with distance from the Galactic Plane. Our simulation shows that brown dwarf population statistics are a function of height above/below the Galactic Plane and sample different age distributions. Interpreting the local sample requires combining evolutionary models, the initial mass function, the star formation history, and kinematic heating. Our models are a guide to how well height-dependent samples can test these scenarios. Sub-populations of brown dwarfs farther from the Plane are older and occupy a different region of brown dwarf parameter space than younger sub-populations closer to the Galactic Plane. Therefore, fully exploring population statistics both near and far from the Plane is critical to prepare for upcoming surveys.

Keywords: Brown dwarfs (185); Solar neighborhood (1509); Luminosity function (942); Stellar populations (1622); Stellar evolutionary models (2046); Sky surveys (1464)

1. INTRODUCTION

The study of brown dwarfs, sub-stellar objects that lack the ability to fuse hydrogen, has been driven by large-scale digital sky surveys for the past 30 years. Originally theorized in 1962 (Kumar 1962), brown dwarfs have been discovered through dedicated surveys with large facilities such as 2MASS (Kirkpatrick et al. 1999; Gizis et al. 2000), PAN-STARRS1 (Deacon et al. 2014; Best et al. 2018), WISE (Cushing et al. 2011; Kirkpatrick et al. 2011), DENIS (Delfosse et al. 1997), SDSS (Leggett et al. 2000), and UKIRT West et al. (2004), but also as foreground contaminants in extragalactic surveys (Hainline et al. 2024; Tee et al. 2023). We are entering

an exciting time for brown dwarf science as the next generation of observation facilities become a reality and start to come online. Observatories such as the James Webb Space Telescope (JWST), Euclid, the Vera C. Rubin Observatory, and the Nancy Grace Roman Space Telescope promise to drastically increase the discovery rate for brown dwarfs and propel the field forward.

Brown dwarfs are cold, sub-stellar objects that extend beyond the main sequence through spectral types L (Martín et al. 1999; Kirkpatrick et al. 1999), T (Burgasser et al. 2002; Geballe et al. 2002), and Y (Delorme et al. 2008; Cushing et al. 2011). These objects have effective temperatures below ~ 2400 , 1300, and 600 K, respectively. As such, these objects are faint in wavelengths shorter than $1 \mu\text{m}$ and present a challenge to observe. Furthermore, since brown dwarfs are not massive enough to fuse hydrogen in their cores, they perpetually

cool and grow dimmer, only increasing the difficulty of their observation.

Brown dwarfs are excellent probes for tracing Galactic evolution and structure (Burgasser 2009). Their kinematics have been used to study their population distributions as well as mapping out the structure of the Milky Way’s thin disk (Faherty et al. 2009; Kirkpatrick et al. 2024). Furthermore, distant M-, L-, and T-type dwarfs can help measure thin disk structure and constrain the thick disk and halo scale heights (Aganze et al. 2022). Therefore, the ability to detect more distant brown dwarfs and understand their formation mechanisms with current and future surveys will play a key role in mapping the Milky Way and advancing such science cases.

Accurately modeling the atmospheres of brown dwarfs is a complicated affair. While their interiors are well known to be fully convective, their atmospheres are complex, filled with molecular features and weather that depend on temperature and pressure evolution (Burrows et al. 2006). The warmer L-dwarfs are covered by cloudy atmospheres, but the observation of these clouds is inclination-dependent (Suárez et al. 2023). As brown dwarfs cool through the L-sequence and into the T-sequence, the clouds sediment and “rain out” minerals and metals leading to clear, cloudless atmospheres (Burrows et al. 2006). These T-dwarfs are further characterized by strong molecular features and the emergence of methane bands in their spectra. Finally, the coolest Y-dwarfs spectral energy peaks at $\sim 5 \mu\text{m}$ and show large spectral absorption features from molecules like water, methane, ammonia, carbon monoxide, and carbon dioxide (Cushing et al. 2011). It appears increasingly likely that late-T and Y dwarf spectra can be described by a second parameter other than temperature, such as metallicity or surface gravity (Beiler et al. 2023). These diverse spectral types are not distinct classifications without overlap, but rather form an evolutionary sequence brown dwarfs undergo as they age and cool. The cooling mechanisms of brown dwarfs are an area of active research for future surveys.

In order to prepare for next-generation surveys that will reveal these dim populations of brown dwarfs and enable the statistical analysis of their characteristics, we must understand their underlying distribution within the Galaxy. We turn to simulating the Solar Neighborhood population of brown dwarfs to predict the characteristics of brown dwarfs that future surveys will see. Previously, the creation of synthetic populations required assuming a birth-rate, star formation rate, and an underlying exponential distribution with height above the Galactic Plane (Ryan et al. 2022). We present a

novel approach using recent Gaia results in conjunction with recent observational relations to build synthetic populations of brown dwarfs.

This paper presents our simulation of Solar Neighborhood brown dwarfs. In Section 2 we build the synthetic population of brown dwarfs. We present the results of the simulation as parameter functions in Section 3. The implications of the results are discussed and compared to recent studies in Section 4. Our conclusions and future work are summarized in Section 5.

2. SIMULATIONS

We simulate synthetic populations of brown dwarfs in the Solar Neighborhood using three different brown dwarf evolutionary models. Starting from observational relations, we assemble the population and apply the evolutionary models to determine the variation of parameters with height above and below the Galactic Plane. Each step in the process is described in detail in the following subsections.

We note that, historically, the Solar Neighborhood refers to a spherical volume ranging from tens to hundreds of parsecs radially from the Sun (Henry et al. 1994; Gaia Collaboration et al. 2021). In this work, we simulate a cylindrical volume that extends above and below the Galactic Plane, but we refer to it as the Solar Neighborhood for simplicity and to emphasize the importance of the growing resolvable volume with future surveys.

2.1. Base Population

Recent analysis of the Solar Neighborhood using Gaia by Mazzi et al. (2024) has revealed the star formation rate (SFR) history for a cylindrical volume centered around the Sun. The cylinder has a radius of 200 pc, is centered on the Galactic Plane, and extends ~ 1300 pc above and below the Plane. This SFR represents the star formation history that produced stellar populations as they are observed today for a given height above and below the Plane. As a result, this does not represent where the stars originally formed, but accounts for kinematic effects. We assume a universal initial mass function such that the brown dwarf formation history follows the stellar formation history.

Positions within the cylinder are denoted by (x, y, z) where x points toward the Galactic center, y points along the Milky Way rotation, and z is perpendicular to the Galactic Plane. We adopt the same coordinate system with the Galactic Plane at $z = 0$ pc and the Sun at $(x, y, z) = (0, 0, 17.7)$ pc, consistent with previous studies (Mazzi et al. (2024), and references therein). The reported SFR history is given as a function of age and z . Temporal bins range from $\log(t \text{ [yr]}) \in [6.6, 10.10]$

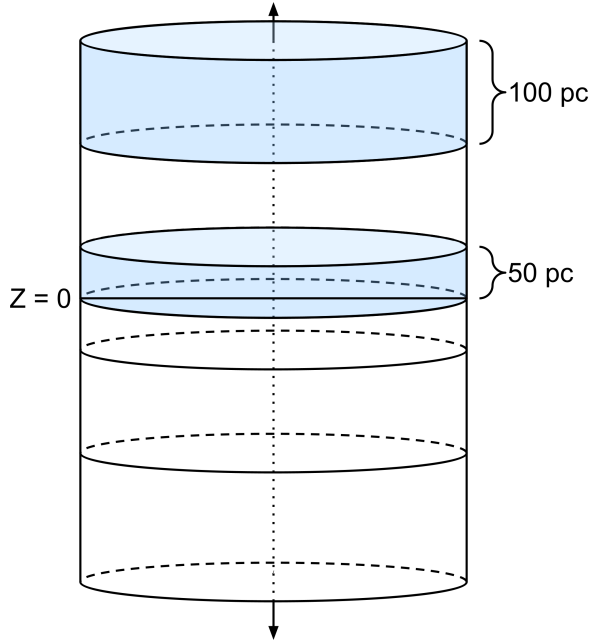


Figure 1. The simulated Solar Neighborhood cylinder with a radius of 200 pc and total height of 2600 pc, 1300 pc above and below the Galactic Plane ($z = 0$). The z -axis is aligned with the cylinder’s vertical axis of symmetry. We divide the cylinder into horizontal slices with smaller $\Delta z = 50$ pc close to the Galactic Plane and more distance slices with larger increments $\Delta z = 100$ pc. This difference allows for higher spatial resolution near the Galactic Plane.

with bin widths of $\Delta \log(t) = 0.2$ for all bins except the first bin, which extends from 6.6 to 7.1. The cylinder is divided into horizontal discs by height above/below the Plane, as shown in Figure 1. Physical slices are in intervals of $\Delta z \approx 50$ pc for $|z| \lesssim 150$ pc and $\Delta z \approx 100$ pc for $150 \text{ pc} \lesssim |z| \lesssim 1300$ pc. In total, there are 16 temporal slices and 28 spatial slices (14 on each side of the Galactic Plane).

For each time and space bin, [Mazzi et al. \(2024\)](#) reports a SFR in $M_{\odot} \text{ yr}^{-1} \text{ kpc}^{-3}$. We normalize the total star formation for each spatial slice (total SFR across all age bins for a given physical slice) using the space density of $1.83 \times 10^{-2} \text{ pc}^{-3}$ from [Best et al. \(2024\)](#), derived from the complete sample of brown dwarfs within 25 pc. We apply this space density to the Solar slice ($0 \leq z \leq 52.63$ pc) and normalize the total SFR for all other slices such that the Solar slice matches observed space densities.

In Figure 2, we show the volume-integrated SFR for the Solar slice and for the entire cylinder. While the full cylinder and the Solar slice have analogous SFR from 3 - 10 Gyr, the Solar slice has a clearly different recent history with a higher proportion of young objects. The

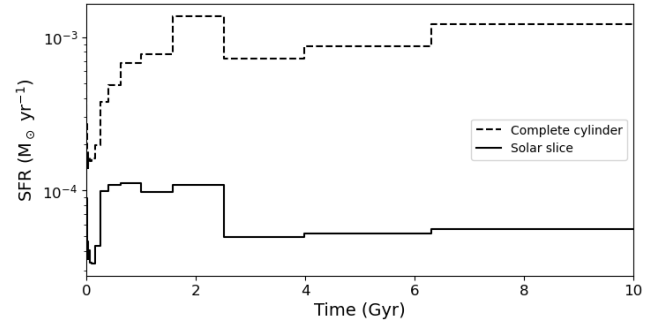


Figure 2. The volume-integrated star formation rate for the Solar slice and complete cylinder. Beyond 2 Gyr ago, the SFR in both cases is nearly identical, but more recently the SFR shows significant differences, with bursty star formation in the Solar slice. The differences in the spatially-correlated SFR underscore the need to use the Gaia-based SFR as opposed to a uniform SFR across the entire cylinder.

spatially-correlated differences in recent star formation demonstrates the importance of using the Gaia-derived SFR history instead of assuming a uniform birth and formation rate.

The total number of simulated objects per physical slice is determined by the normalized SFR. We uniformly assign positions to objects within a physical slice and calculate the ages of objects by proportionally dividing the total number of objects within the physical slice by the SFR for each temporal bin. Within a temporal bin, object ages are uniformly distributed.

Object positions in (x, y, z) are translated to Galactic l, b and distance from the Sun (D_{obs}) where:

$$\begin{aligned} D_{obs} &= \sqrt{x^2 + y^2 + (z - 17.7)^2}, \\ b &= \arcsin((z - 17.7)/D_{obs}), \\ l &= \text{sgn}(y) * \arccos(x/\sqrt{x^2 + y^2}). \end{aligned} \quad (1)$$

In cases where $(x, y) = (0, 0)$, l is undefined and we manually set $l = 0^\circ$. Further transformations from Galactic to other coordinate frames, such as the standard RA/Dec (FK5), are done through [Astropy](#)¹ ([Astropy Collaboration et al. 2013, 2018, 2022](#)). The distribution of objects in 100 pc bins is shown in Figure 3, where slices closest to the Galactic Plane have a higher number density as set by the normalized SFR.

The final two base parameters of the synthetic population are object masses and metallicities. Masses are distributed based on the Initial Mass Function (IMF) from [Kirkpatrick et al. \(2021\)](#):

$$\frac{dN}{dM} \propto M^{-\alpha}, \quad (2)$$

¹ <https://www.astropy.org/>

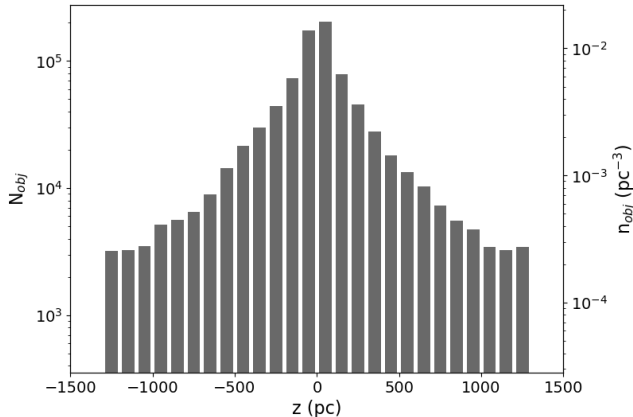


Figure 3. The number and spatial densities of simulated objects per 100 pc interval are shown. The number of objects per interval was obtained by normalizing the SFR history to the local sample. Objects are concentrated at low $|z|$ values and have lower spatial densities farther from the Plane.

where $\alpha = 0.6 \pm 0.1$. We allow masses to range from $0.003 - 0.08 M_{\odot}$.

Metallicities are assigned to the population using the Age-Metallicity Relation (AMR) from [Dal Tio et al. \(2021\)](#):

$$[Fe/H] = \beta(t - 4.5 \text{ Gyr}), \quad (3)$$

where $\beta = -0.4 \text{ dex}/12 \text{ Gyr}$. We include gaussian scatter with $\sigma = 0.1$. This AMR assigns solar metallicities to solar-aged objects whereas older objects are more metal-poor.

The SFR, IMF, and AMR can be combined to obtain object positions, ages, masses, and metallicities, the base parameters of our synthetic populations. The total number of objects in the base simulation, normalized using the local brown dwarf volume density, is $\sim 820,000$. The objects form a complete simulated cylinder around the Solar Neighborhood, but lack evolutionary parameters such as effective temperatures, radii, surface gravities, and luminosities.

2.2. Evolutionary Model Application

From the base catalog created in Section 2.1, we apply three different models to “evolve” the synthetic population. We apply two of the Sonora substellar atmosphere models: Bobcat ² ([Marley et al. 2021](#)) and Diamondback³ ([Morley et al. 2024](#)). The third model we apply is the 2008 hybrid model from [Saumon & Marley \(2008\)](#) (hereafter SM08).

² <https://zenodo.org/records/5063476>

³ <https://zenodo.org/records/12735103>

The Bobcat models describe cloudless, substellar objects with near-solar metallicities. The Diamondback models are a hybrid model that includes a gravity-dependent transition from cloudy to cloudless models between 1000 and 1300 K. Below 900 K, the Diamondback evolutionary models use the Bobcat models. The Sonora atmospheric model suite provides atmospheric structure, spectra, chemistry, and evolutionary tables for substellar objects. The evolutionary tables contain effective temperature, radius, luminosity, surface gravity, mass, age, and metallicity. The SM08 models are similar, incorporating a hybrid transition from cloudy to cloudless at 1400 K, but the SM08 evolutionary model assumes solar metallicity and does not have a model spectral grid.

For each evolutionary model, we linearly interpolate the ages, masses, and metallicities of the base population to retrieve effective temperatures, radii, surface gravities, and luminosities. For the SM08 evolved population, we only interpolate the base population’s ages and masses since solar metallicity is assumed. Objects with parameters beyond the evolutionary model grids are removed from the sample to avoid unphysical extrapolation.

From the three evolved populations, we explore how different parameters, such as luminosity and age, vary as a function of z .

3. RESULTS

In this section, we present the outputs of our simulated Solar Neighborhood population. We explore the distribution of objects and their parameters for all three synthetic populations. The variation of evolutionary parameters with height above and below the Galactic Plane, $|z|$, is of particular interest.

3.1. Age Distribution

Object ages form part of the base parameters for the simulation and are identical for all three synthetic populations. In general, objects with smaller $|z|$ values, i.e. closer to the Plane, are younger whereas more distant objects are older. This trend is true for all time bins as seen in Figure 4. Furthermore, the SFR shows a decrease from 4 to 8 Gyr ago before undergoing a recent burst of star formation from 3 Gyr to the present. Figure 4 shows older objects (≥ 7 Gyr) are more evenly distributed across z values whereas younger objects (≤ 3 Gyr) are almost exclusively found within 300 pc from the Galactic Plane. The distribution of young and old objects supports an interpretation of dynamical heating of the Galactic Plane, which removes objects from the Plane over time, spreading older populations out to

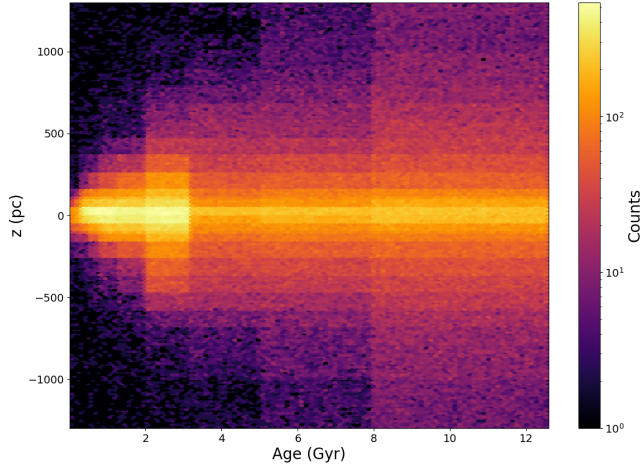


Figure 4. The age distribution of the base population as a function of distance from the Galactic Plane, z , is shown. The same age distribution is used for all three synthetic populations. Ages were assigned directly from the SFR history; for a given age, z positions with higher counts are a direct result of higher SFR. The age distribution shows a decline in SFR between 4 - 8 Gyr ago with a recent burst of star formation around the Galactic Plane.

higher $|z|$ values (Spitzer & Schwarzschild 1953; Lacey 1984; Sellwood & Binney 2002; Ma et al. 2017).

3.2. Temperature Function

Object temperatures are obtained by linearly interpolating the base population’s age, mass, and metallicity for both Sonora models and interpolating the base population’s age and mass for the SM08 model. The resulting distributions of all simulated object temperatures are shown in Figure 5.

Interpolated Sonora Bobcat population temperatures are smoothly distributed, favoring lower temperatures. The SM08 derived temperatures also favor lower temperatures but have an additional feature centered at 1400 K, surrounding the transition point between cloudy and cloudless atmospheres. This pileup was predicted and discussed in detail by Saumon & Marley (2008). The pileup is nonexistent in the Sonora Bobcat temperatures as the models are exclusively cloudless. The Sonora Diamondback models show a prominent transition feature more sharply concentrated at 1300 K. The Diamondback cloudy-clear atmospheric transition occurs at a cooler temperature than the SM08 transition.

At temperatures cooler than the atmospheric transition pileups, the Bobcat and Diamondback models are similar, with the Diamondback model predicting slightly more of the coldest objects ($T_{\text{eff}} < 400$ K) than the Bobcat model. The SM08 model grid does not extend below $T_{\text{eff}} = 275$ K. As such, linear interpolation for the coldest objects results in an unphysical pileup at the bot-

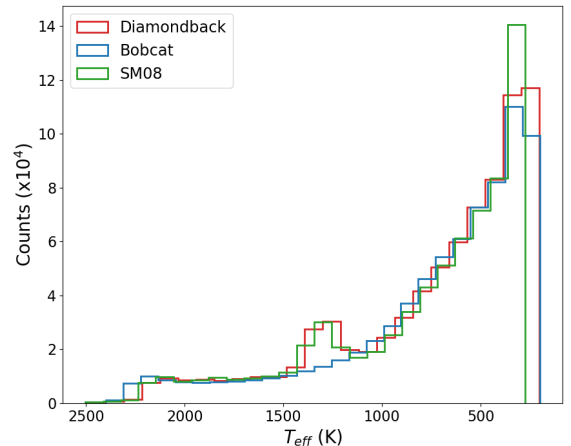


Figure 5. Cumulative effective temperature distribution for all three synthetic populations over the entire simulated volume. The hybrid Diamondback (red) and SM08 (green) models show object pileup as the models transition from cloudy to clear atmospheres. The central peak and width of these features differ based on the interpolation-based and gravity-dependent approaches taken by SM08 and Diamondback, respectively. All three models favor cooler objects below 1000 K.

tom edge of the model grid. Therefore, the overdensity shown in Figure 5 between 300 - 400 K for the SM08 model should be interpreted as a numerical artifact and not a physical effect.

3.3. Luminosity Function

The luminosity function is arguably the most important of the parameter functions as it is the only one that is directly observable; in practice, ultracool dwarf parameters are obtained by measuring an object’s luminosity and applying evolutionary models to recover remaining parameters. Additionally, synthetic luminosity functions can be compared to observational luminosity functions to constrain ultracool dwarf cooling mechanisms.

In Figure 6, we display the cumulative luminosity function of all three synthetic populations. Plotting the luminosity function as a function of z allows us to separate the contributions from different distances above/below the Galactic Plane. We show the SM08 hybrid model’s luminosity function as it varies with z in Figure 7 but leave the Sonora Bobcat and Diamondback luminosity functions’ z dependence to be explored in more detail in Section 4.

To facilitate comparison with previous studies and observations, we also plot the luminosity function in bolometric magnitudes. We converted interpolated luminosities to bolometric magnitudes using $M_{\text{bol},\odot} = 4.740$

mag:

$$M_{bol} = M_{bol,\odot} - 2.5 \log(L/L_{\odot}). \quad (4)$$

As shown in Figure 6, both hybrid models have prominent transition pileup features before favoring less luminous objects. The amplitude and width of the pileup feature is significantly larger for the Diamondback model than the SM08 model. These differences reflect the gravity-dependent nature of the Diamondback transition, where the transition phase lasts longer for lower surface gravities. For both the SM08 and Diamondback models, the transition occurs at $\log(L/L_{\odot}) \sim -4.7$ or $M_{bol} \approx 16.25$ mag. All three models favor lower luminosities and have increased counts concentrated around $\log(L/L_{\odot}) \approx -6.3$, or $M_{bol} \approx 20.5$ mag. The SM08 models do not extend below $\log(L/L_{\odot}) = -7.3$, or $M_{bol} = 23$ mag. As previously seen in the temperature distribution, an additional pileup of objects interpolated at the edge of the SM08 model grid appears at $M_{bol} = 23$ mag, but is unphysical.

Recent analysis of ultracool dwarfs within 25 pc by Best et al. (2024) yields an observed bolometric luminosity function that is flat from $M_{bol} = 16 - 20$ mag and then peaks from $M_{bol} = 20 - 22$ mag. However, magnitudes fainter than $M_{bol} = 21$ mag are not well measured to date. Our luminosity function does not reproduce the observed flat region between $M_{bol} = 16 - 20$ mag, but does reach a maximum by $M_{bol} \approx 20$ mag. Our simulations are in agreement with the models shown in Best et al. (2024).

Additional pileup features in the Diamondback distribution can be seen at $M_{bol} = 22$ and 24 mag. While the latter may be an effect of interpolation, the former may be related to the transition from T to Y spectral types. This feature is larger than the Poisson noise of the simulation. From effective temperature-spectral type relations in Kirkpatrick et al. (2021), Y-dwarfs have $T_{\text{eff}} \leq 460$ K. For the Diamondback model, objects with temperatures below 460 K have $\log(L/L_{\odot}) \leq -6.5$. One possible physical explanation of the secondary pileup feature is the emergence of water features in Y-dwarf atmospheres after the T-Y transition. However, as stated in Marley et al. (2021), this interpretation should be used with caution as the Bobcat models do include water condensation effects but not the associated cloud opacity that follows.

One advantage to our simulation is we are able to show the distribution of luminosities as a function of position above/below the Galactic Plane, as shown in Figure 7 for the SM08 population (see Figure 10 for the Sonora model-based populations). The same features seen in Figure 6 for the SM08 luminosity function, primarily the pileup feature at $\log(L/L_{\odot}) = -4.7$ as well as the

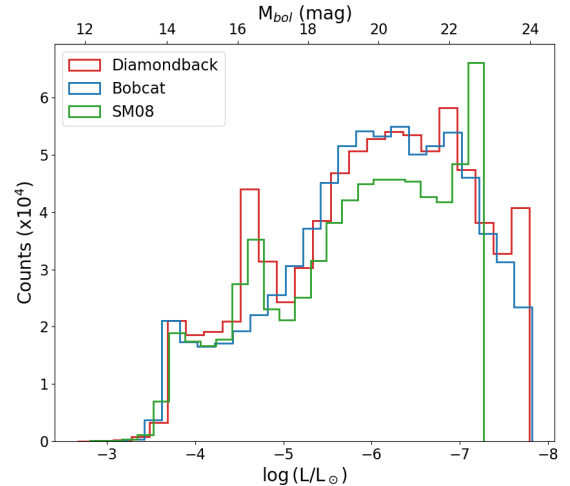


Figure 6. Cumulative luminosity and bolometric magnitude distributions for all three synthetic populations over the entire simulated volume. Both the Diamondback (red) and SM08 (green) hybrid models show an atmospheric transition pileup while the cloudless Bobcat models (blue) do not. The Diamondback model shows an additional feature at $M_{bol} = 22$ mag unseen in the SM08 models. All three models favor objects with lower luminosities between $\log(L/L_{\odot}) = -5.5$ and -7.5 .

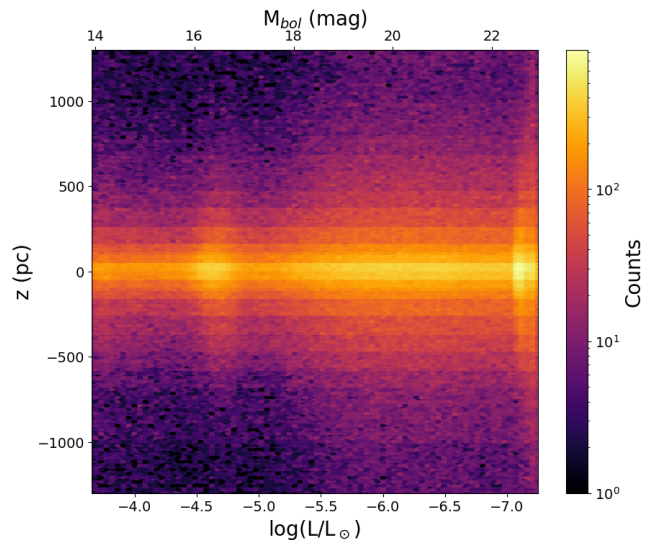


Figure 7. The SM08 synthetic population's luminosity function with respect to position above/below the Galactic Plane. Bolometric magnitudes are also shown for convenience. The pileup from atmospheric modeling transitions is prominently visible at $\log(L/L_{\odot}) \approx 4.6$ and extends approximately 500 pc both above and below the Plane before gradually disappearing. An additional concentration of objects is seen at the lowest luminosities ($M_{bol} \geq 22$ mag) near the Plane, however this grouping of objects is likely a non-physical pileup at the edge of the model grid.

concentration at lower luminosities, present themselves in Figure 7. However, by showing the luminosity function with object z positions, it is clear that the transition pileup at brighter luminosities does not extend as far out from the Galactic Plane as the lower luminosity object concentration; the transition pileup feature is primarily seen within 500 pc above/below the Galactic Plane and is nearly non-existent beyond 1 kpc. On the contrary, the distribution of lower luminosity objects is significantly more widespread, reaching well beyond 1 kpc above/below the Galactic Plane. In other words, *the luminosity function for a subset of objects is dependent on the objects' vertical distance from the Galactic Plane.* This result has important implications for future astronomical surveys as technological advancements allow observers to probe more distant populations of ultracool dwarfs.

4. DISCUSSION

In this section, we first compare our synthetic populations with the most complete brown dwarf sample to-date. Then, we discuss object parameter functions from our simulation and their dependence on $|z|$. Finally, we comment on the implications of our findings for future surveys.

4.1. Comparison with Observations

To compare our synthetic populations with local observational samples, we calculate the number of simulated objects per spectral type within 25 pc for all three synthetic populations using the effective temperature-spectral type polynomial relation from Kirkpatrick et al. (2021). The resulting counts are shown in Figure 8. For observational comparison, we use completeness-corrected space densities from Best et al. (2024) and calculate expected counts within the 25 pc sphere. The results are shown in black with Poisson errors in Figure 8.

Across all spectral types, all three model populations perform similarly, with the exception of the cloudless Sonora Bobcat population over small intervals (L6 - L8 and T6 - T7). The hybrid populations (Sonora Diamondback and SM08) are in agreement with each other for all spectral types. For early to mid L-types, the models are in agreement with observations with the exception of L5, where all three models underpredict the number of L5 dwarfs. All three models are in agreement with observations for L7 types, but struggle to match observations in later L-types. Both hybrid models overpredict L8 dwarfs while the cloudless Bobcat models underpredict L8 dwarfs, and all three models underpredict L9 types. The sudden shift from hybrid models overpredicting L8 types to underpredicting L9 types stems from

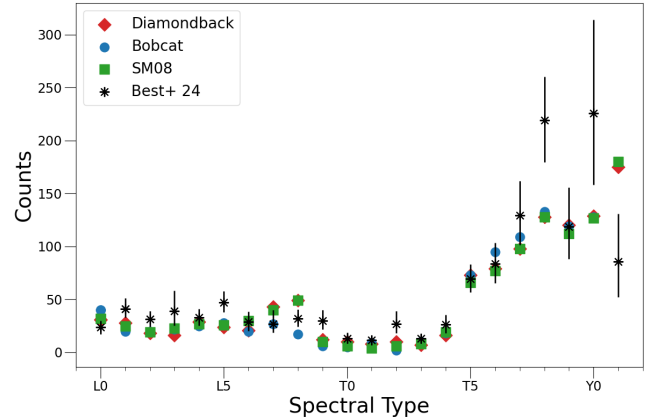


Figure 8. Simulated object counts within 25 pc by spectral type are shown in red diamonds (Sonora Diamondback), blue circles (Sonora Bobcat), and green squares (SM08). We compare to calculated counts from Best et al. (2024) corrected space densities with Poisson errors, denoted by black stars. All three synthetic populations are in agreement with observations for early L-type dwarfs and over-predict the late L-types before being in agreement with the observations for early T-type brown dwarfs. Conservatively, observations beyond T5 spectral types are poorly constrained and limit comparability.

the transition from cloudy to cloudless atmospheres; the SM08 models transition at 1400 K while the Sonora Diamondback models transition at 1300 K, which both occur between spectral types L7 - L9.

Our simulations agree with observations for T-dwarfs out to T7 aside from a spike in the observational counts of T2 dwarfs. All three models perform nearly identically over the T0 - T5 range; this is expected since early T-dwarfs are well characterized by cloudless atmospheres. For late T-type dwarfs, Best et al. (2024) urge caution as the space densities are derived from significantly incomplete samples. However, to first order, we expect the number of objects in the coldest spectral types to increase as formation mechanisms favor lower mass objects and older objects continually cool. Thus, the increase in counts for synthetic populations beyond T8 dwarfs is plausible. A more complete sample of late T-dwarfs and Y-dwarfs is necessary to constrain the low temperature end of our population model.

4.2. Fundamental Parameter Functions

As future observatories, such as JWST, Euclid, Rubin, and Roman commence operations and detect brown dwarfs all the way into the Galactic Halo, the effects of Galactic dynamics can no longer be ignored. For small, Solar Neighborhood samples, the overall kinematics and observational effects from the Galaxy as a whole could

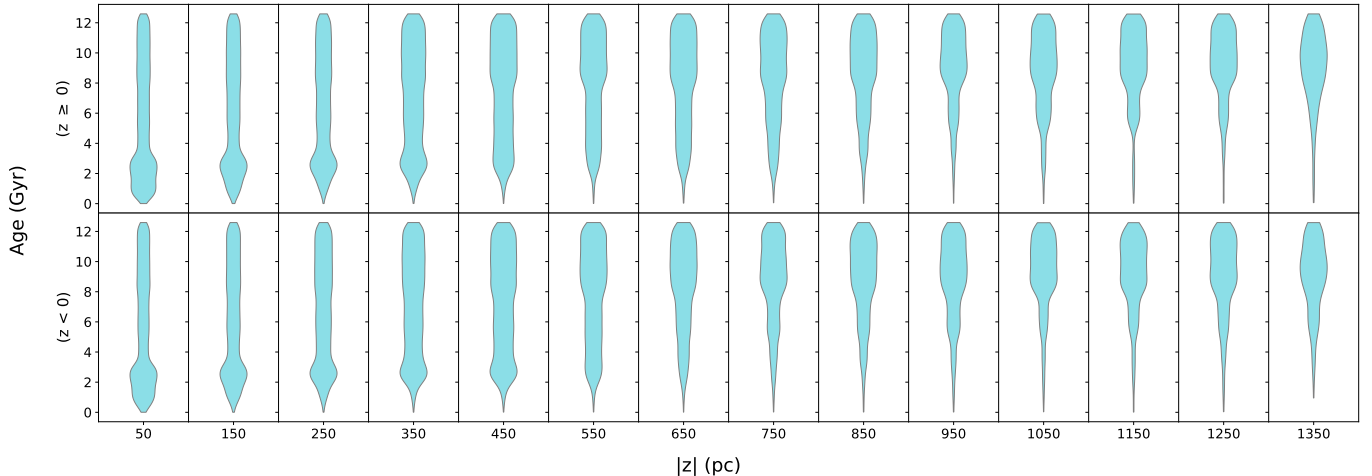


Figure 9. The age distribution in 100 pc intervals. The upper row of panels correspond to positions above the Plane while the lower row corresponds to positions below the Plane. The age distributions of objects (and by extension the SFR history) is nearly symmetric above and below the Plane. Physical slices closest to the Plane are dominated by younger ages whereas slices farther from the Plane contain progressively older populations.

be minimized, but such an approach will no longer be possible for larger, more distant samples.

Our simulation presents the current state of brown dwarfs within 200 pc and 1.3 kpc above/below the Galactic Plane. Whereas local samples are inherently biased towards young objects, since older objects have higher velocities from dynamical heating (Kirkpatrick et al. 2021), our simulation inherently accounts for these kinematics by using the Gaia-derived SFR history. As such, our simulation yields the number of objects and their ages as one would find them today, accounting for Galactic effects. We capture the older populations at higher $|z|$ values as well as the young populations close to the Galactic Plane. Figure 9 shows how the distribution of object ages changes by 100 pc slices above and below the Plane. Slices near the Galactic Plane favor younger objects and slices farther from the Plane progressively favor older objects; the most distant slices are almost entirely comprised of old (≥ 8 Gyr) objects. This trend appears both above and below the Galactic Plane with only slight differences in slices at comparable $|z|$ heights. Note that the final slice, $|z| \geq 1.3$ kpc shows a slightly younger distribution than the previous slice, but this is a numerical effect from small number statistics as the simulation does not encompass the entire 1.3 - 1.4 kpc slice but rather only reaches $|z| \approx 1.32$ kpc. Only ~ 500 objects fall into each of the most distant, incomplete bins above/below the Plane.

Future surveys that will probe farther beyond the Galactic Plane will see combinations of these age distributions. Understanding the underlying relation between $|z|$ and age is key to interpreting the observed luminosity function and evolution of the brown dwarf population.

Complete observational samples to date only extend to the nearest, youngest slices in our simulation. Local samples are biased against older objects, which is problematic in interpreting brown dwarf formation mechanisms. By extending our simulation to higher distances above/below the Galactic Plane, we include older objects that are underrepresented in the local sample.

Coupled with age, our simulation includes metallicity predictions stemming from the Dal Tio et al. (2021) age-metallicity relation (Equation 3). As a consequence of more distant slices being older on average, sub-populations farther from the Galactic Plane are more metal poor whereas the younger objects closer to the Plane are closer to Solar metallicity. Older populations are expected to be more metal poor than younger populations due to supernovae feedback, multiple stellar populations, and metallicity enrichment around the dusty, gaseous Galactic Plane. Our simulation is in good agreement with these expectations and we find the oldest sub-populations, most distant from the Plane, are more metal poor than the younger sub-populations near the Plane.

In Figure 10, we show the evolution of the Sonora Diamondback and Bobcat luminosity functions in 100 pc intervals above/below the Galactic Plane. Similar to the spatially-resolved luminosity function for SM08 in Figure 7, the Sonora luminosity function morphologies and feature strengths change with $|z|$. Specifically, the Diamondback cloudy-cloudless transition feature is prominent in sub-populations near the Galactic Plane but decreases in amplitude as $|z|$ increases, becoming nearly indistinguishable beyond 700 pc. Similarly, the T-Y transition is only visible within 400 pc of the Plane.

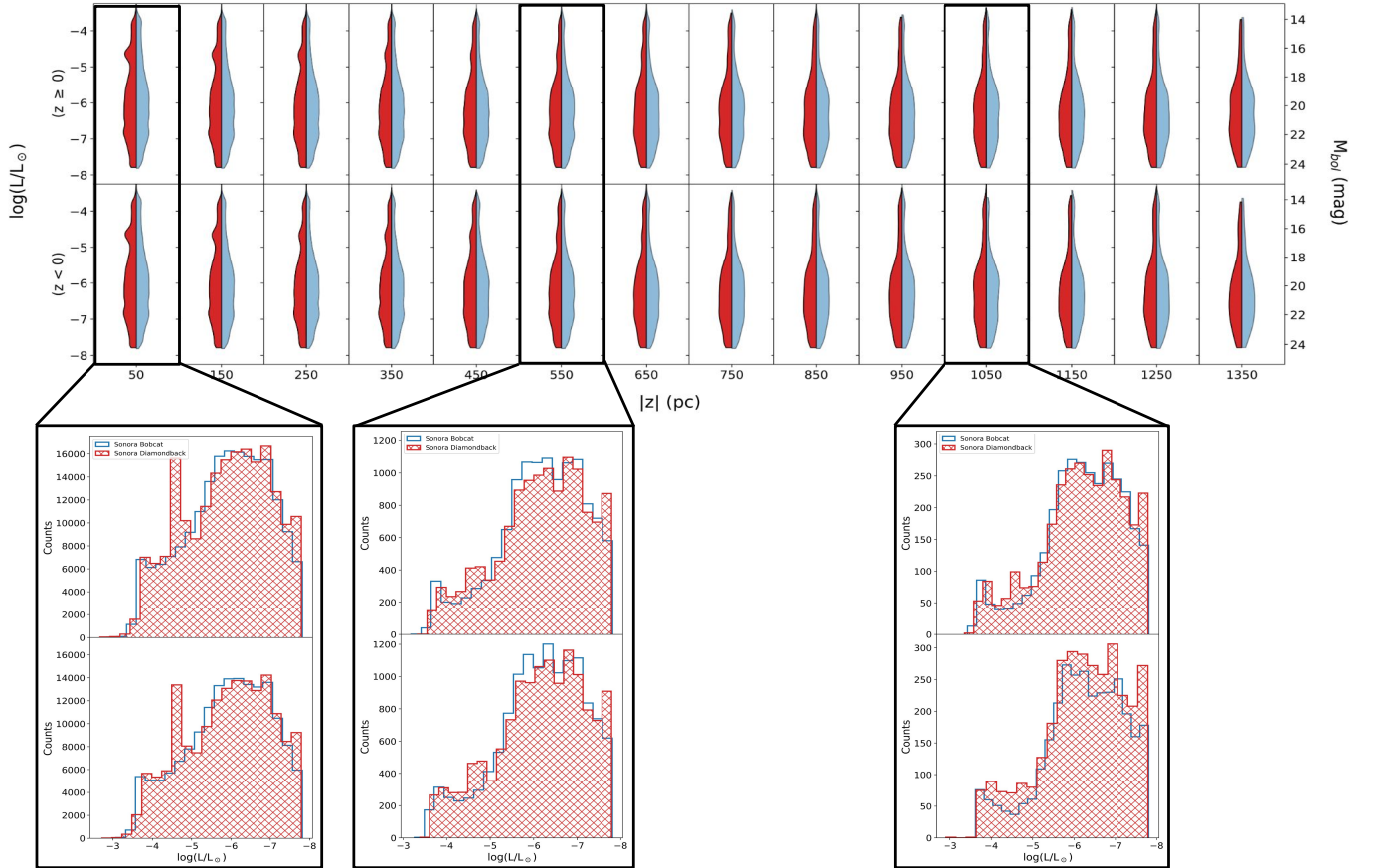


Figure 10. The luminosity function for the Sonora Diamondback (red) and Bobcat (blue) synthetic populations is shown in 100 pc bins. As distance from the Plane increases, the cloudy-cloudless transition feature in the Diamondback model dissipates and the population shifts to the lowest luminosities. In the slices closest to the Galactic Plane, the T-Y transition pileup is visible but is indistinguishable at larger distances. The Bobcat luminosity function is smooth but extends to brighter luminosities at $|z|$ slices. Three slices are shown in greater detail in pop-out histograms. The histograms closest to the Galactic Plane (far left) contain more objects and show the most prominent pileup features. The middle pop-out contains fewer objects and shows the decrease in pileup feature strength. The farthest pop-out from the Plane (far right) contains the least number of objects and the weakest pileup feature strength.

For both Sonora models, the luminosity function morphology becomes more compact around lower luminosities as distance from the Plane increases.

The detailed histograms of each 100 pc interval’s luminosity function (shown as pop-outs in Figure 10), show the sub-population luminosity functions in finer detail and that the feature strengths and overall distribution changes significantly with $|z|$. Furthermore, intervals closest to the Galactic Plane contain the highest number of objects and are primarily younger. Thus, the contribution of slices near the Plane to the total luminosity function is greater and enhances the strength of the cloudy-cloudless transmission feature.

Since the luminosity function can be used to probe the cooling mechanisms and interior physics of brown dwarfs, improperly accounting for contributions from the more numerous, nearby young objects and the less

numerous, farther older objects could lead to misinterpreting the physics of brown dwarfs. By including older populations more distant from the Galactic Plane, our simulation offers a novel approach to understanding a broader range of brown dwarf parameters than currently allowed by local samples.

Understanding the evolution of the luminosity function with height above and below the Galactic Plane is of particular importance to accurately describe the ages, masses, and fundamental properties of ultracool dwarfs. The ages, masses, and luminosities of ultracool dwarfs are degenerate, so it is exceptionally challenging, if not impossible, to age these objects to understand their evolution (Faherty 2014; Dupuy & Liu 2017). However, by dividing the Solar Neighborhood into respective slices with individual luminosity functions, the observed luminosity function can be compared with predicted func-

tions and the contributions from different aged objects in various slices can be quantified.

5. SUMMARY

We have simulated brown dwarfs in the Solar Neighborhood using Gaia-based star formation rate history both above and below the Galactic Plane. This novel approach allows us to measure the population statistics as a function of height and sample different age distributions. Normalized to the local brown dwarf spatial density, our simulation predicts the physical distribution, ages, and metallicities of brown dwarfs within a cylinder centered on the Galactic Plane. Our simulation predicts $\sim 820,000$ brown dwarfs are encapsulated within such a cylinder and are concentrated near the Galactic Plane. We apply the hybrid SM08, gravity-dependent hybrid Sonora Diamondback, and cloudless Sonora Bobcat evolutionary models to our synthetic population to obtain effective temperatures, radii, surface gravities, and luminosities. The temperature and luminosity functions favor cooler, dimmer objects at all slices, but warmer, more luminous sub-populations appear near the Galactic Plane. The hybrid models include a characteristic pileup of objects around 1300 - 1400 K as the models transition from cloudy to cloudless. The pileup is a prominent feature for slices near the Galactic Plane but dissipates for more distant slices.

Understanding the underlying luminosity function as future surveys detect more distant objects is critical as the luminosity function is the only directly observable parameter – all other object parameters, such as mass, temperature, and radius are model-derived quantities based on luminosity. By creating multiple evolutionary model luminosity functions, we can compare with the observed luminosity functions to understand brown dwarf evolution and cooling mechanisms. Our simula-

tion accounts for older objects that are underrepresented in local samples, which adds significant, previously unavailable information for interpreting brown dwarf formation mechanisms. Furthermore, more distant populations within our simulation are older and more metal poor, a result that points to dynamical heating and Galactic dynamics.

We reach a seemingly trivial, yet critical takeaway: *As surveys resolve more distant populations of brown dwarfs, luminosity functions will sum along the line of sight. Therefore, it will become increasingly important to disentangle the contributions from older populations more distant from the Galactic Plane to properly understand brown dwarf cooling and formation mechanisms.*

The next paper in this series will apply photometric survey footprints and nominal depths to the synthetic population to predict detection counts and population completeness. Future surveys such as JWST, Euclid, Rubin, and Roman will enable the statistical analysis of brown dwarf populations and will measure space densities as a function of height that can be compared to our predictions.

ACKNOWLEDGMENTS

The authors thank Leo Girardi and Alessandro Mazzi for email exchange in applying their results to this simulation. The authors also thank University of Delaware's Tali Natan, Sid Chiani, and FAST Lab for feedback on visualization approaches and figures. EJH is supported by NASA EPSCoR R3 award 80NSSC24M0160.

Software: `astropy` (Astropy Collaboration et al. 2013, 2018, 2022), `Jupyter` (Kluyver et al. 2016), `NumPy` (Harris et al. 2020), `matplotlib` (Hunter 2007), `statsmodels` (Seabold & Perktold 2010), `SciPy` (Virtanen et al. 2020), and `Python3` (Van Rossum & Drake 2009).

REFERENCES

- Aganze, C., Burgasser, A. J., Malkan, M., et al. 2022, *ApJ*, 934, 73, doi: [10.3847/1538-4357/ac7053](https://doi.org/10.3847/1538-4357/ac7053)
- Astropy Collaboration, Robitaille, T. P., Tollerud, E. J., et al. 2013, *A&A*, 558, A33, doi: [10.1051/0004-6361/201322068](https://doi.org/10.1051/0004-6361/201322068)
- Astropy Collaboration, Price-Whelan, A. M., Sipőcz, B. M., et al. 2018, *AJ*, 156, 123, doi: [10.3847/1538-3881/aabc4f](https://doi.org/10.3847/1538-3881/aabc4f)
- Astropy Collaboration, Price-Whelan, A. M., Lim, P. L., et al. 2022, *ApJ*, 935, 167, doi: [10.3847/1538-4357/ac7c74](https://doi.org/10.3847/1538-4357/ac7c74)
- Beiler, S. A., Cushing, M. C., Kirkpatrick, J. D., et al. 2023, *ApJL*, 951, L48, doi: [10.3847/2041-8213/ace32c](https://doi.org/10.3847/2041-8213/ace32c)
- Best, W. M. J., Sanghi, A., Liu, M. C., Magnier, E. A., & Dupuy, T. J. 2024, *ApJ*, 967, 115, doi: [10.3847/1538-4357/ad39ef](https://doi.org/10.3847/1538-4357/ad39ef)
- Best, W. M. J., Magnier, E. A., Liu, M. C., et al. 2018, *ApJS*, 234, 1, doi: [10.3847/1538-4365/aa9982](https://doi.org/10.3847/1538-4365/aa9982)
- Burgasser, A. J. 2009, in *The Ages of Stars*, ed. E. E. Mamajek, D. R. Soderblom, & R. F. G. Wyse, Vol. 258, 317–326, doi: [10.1017/S1743921309031974](https://doi.org/10.1017/S1743921309031974)
- Burgasser, A. J., Kirkpatrick, J. D., Brown, M. E., et al. 2002, *ApJ*, 564, 421, doi: [10.1086/324033](https://doi.org/10.1086/324033)
- Burrows, A., Sudarsky, D., & Hubeny, I. 2006, *ApJ*, 640, 1063, doi: [10.1086/500293](https://doi.org/10.1086/500293)

- Cushing, M. C., Kirkpatrick, J. D., Gelino, C. R., et al. 2011, *ApJ*, 743, 50, doi: [10.1088/0004-637X/743/1/50](https://doi.org/10.1088/0004-637X/743/1/50)
- Dal Tio, P., Mazzi, A., Girardi, L., et al. 2021, *MNRAS*, 506, 5681, doi: [10.1093/mnras/stab1964](https://doi.org/10.1093/mnras/stab1964)
- Deacon, N. R., Liu, M. C., Magnier, E. A., et al. 2014, *ApJ*, 792, 119, doi: [10.1088/0004-637X/792/2/119](https://doi.org/10.1088/0004-637X/792/2/119)
- Delfosse, X., Tinney, C. G., Forveille, T., et al. 1997, *A&A*, 327, L25
- Delorme, P., Delfosse, X., Albert, L., et al. 2008, *A&A*, 482, 961, doi: [10.1051/0004-6361:20079317](https://doi.org/10.1051/0004-6361:20079317)
- Dupuy, T. J., & Liu, M. C. 2017, *ApJS*, 231, 15, doi: [10.3847/1538-4365/aa5e4c](https://doi.org/10.3847/1538-4365/aa5e4c)
- Faherty, J. K. 2014, *Mem. Soc. Astron. Italiana*, 85, 725
- Faherty, J. K., Burgasser, A. J., Cruz, K. L., et al. 2009, *AJ*, 137, 1, doi: [10.1088/0004-6256/137/1/1](https://doi.org/10.1088/0004-6256/137/1/1)
- Gaia Collaboration, Smart, R. L., Sarro, L. M., et al. 2021, *A&A*, 649, A6, doi: [10.1051/0004-6361/202039498](https://doi.org/10.1051/0004-6361/202039498)
- Geballe, T. R., Knapp, G. R., Leggett, S. K., et al. 2002, *ApJ*, 564, 466, doi: [10.1086/324078](https://doi.org/10.1086/324078)
- Gizis, J. E., Monet, D. G., Reid, I. N., et al. 2000, *AJ*, 120, 1085, doi: [10.1086/301456](https://doi.org/10.1086/301456)
- Hainline, K. N., Helton, J. M., Johnson, B. D., et al. 2024, *ApJ*, 964, 66, doi: [10.3847/1538-4357/ad20d1](https://doi.org/10.3847/1538-4357/ad20d1)
- Harris, C. R., Millman, K. J., van der Walt, S. J., et al. 2020, *Nature*, 585, 357, doi: [10.1038/s41586-020-2649-2](https://doi.org/10.1038/s41586-020-2649-2)
- Henry, T. J., Kirkpatrick, J. D., & Simons, D. A. 1994, *AJ*, 108, 1437, doi: [10.1086/117167](https://doi.org/10.1086/117167)
- Hunter, J. D. 2007, *Computing in Science & Engineering*, 9, 90, doi: [10.1109/MCSE.2007.55](https://doi.org/10.1109/MCSE.2007.55)
- Kirkpatrick, J. D., Reid, I. N., Liebert, J., et al. 1999, *ApJ*, 519, 802, doi: [10.1086/307414](https://doi.org/10.1086/307414)
- Kirkpatrick, J. D., Cushing, M. C., Gelino, C. R., et al. 2011, *ApJS*, 197, 19, doi: [10.1088/0067-0049/197/2/19](https://doi.org/10.1088/0067-0049/197/2/19)
- Kirkpatrick, J. D., Gelino, C. R., Faherty, J. K., et al. 2021, *ApJS*, 253, 7, doi: [10.3847/1538-4365/abd107](https://doi.org/10.3847/1538-4365/abd107)
- Kirkpatrick, J. D., Marocco, F., Gelino, C. R., et al. 2024, *ApJS*, 271, 55, doi: [10.3847/1538-4365/ad24e2](https://doi.org/10.3847/1538-4365/ad24e2)
- Kluyver, T., Ragan-Kelley, B., Pérez, F., et al. 2016, in *Positioning and Power in Academic Publishing: Players, Agents and Agendas*, ed. F. Loizides & B. Schmidt, IOS Press, 87 – 90
- Kumar, S. S. 1962, *Astronomical Journal*, 67, 579, doi: [10.1086/108658](https://doi.org/10.1086/108658)
- Lacey, C. G. 1984, *MNRAS*, 208, 687, doi: [10.1093/mnras/208.4.687](https://doi.org/10.1093/mnras/208.4.687)
- Leggett, S. K., Geballe, T. R., Fan, X., et al. 2000, *ApJL*, 536, L35, doi: [10.1086/312728](https://doi.org/10.1086/312728)
- Ma, X., Hopkins, P. F., Wetzel, A. R., et al. 2017, *MNRAS*, 467, 2430, doi: [10.1093/mnras/stx273](https://doi.org/10.1093/mnras/stx273)
- Marley, M. S., Saumon, D., Visscher, C., et al. 2021, *ApJ*, 920, 85, doi: [10.3847/1538-4357/ac141d](https://doi.org/10.3847/1538-4357/ac141d)
- Martín, E. L., Delfosse, X., Basri, G., et al. 1999, *AJ*, 118, 2466, doi: [10.1086/301107](https://doi.org/10.1086/301107)
- Mazzi, A., Girardi, L., Trabucchi, M., et al. 2024, *MNRAS*, 527, 583, doi: [10.1093/mnras/stad2952](https://doi.org/10.1093/mnras/stad2952)
- Morley, C. V., Mukherjee, S., Marley, M. S., et al. 2024, *arXiv e-prints*, arXiv:2402.00758, doi: [10.48550/arXiv.2402.00758](https://doi.org/10.48550/arXiv.2402.00758)
- Ryan, R. E., Thorman, P., Aganze, C., et al. 2022, 932, 96, doi: [10.3847/1538-4357/ac6de5](https://doi.org/10.3847/1538-4357/ac6de5)
- Saumon, D., & Marley, M. S. 2008, *ApJ*, 689, 1327, doi: [10.1086/592734](https://doi.org/10.1086/592734)
- Seabold, S., & Perktold, J. 2010, in *9th Python in Science Conference*
- Sellwood, J. A., & Binney, J. J. 2002, *MNRAS*, 336, 785, doi: [10.1046/j.1365-8711.2002.05806.x](https://doi.org/10.1046/j.1365-8711.2002.05806.x)
- Spitzer, Lyman, J., & Schwarzschild, M. 1953, *ApJ*, 118, 106, doi: [10.1086/145730](https://doi.org/10.1086/145730)
- Suárez, G., Vos, J. M., Metchev, S., Faherty, J. K., & Cruz, K. 2023, *ApJL*, 954, L6, doi: [10.3847/2041-8213/acec4b](https://doi.org/10.3847/2041-8213/acec4b)
- Tee, W. L., Fan, X., Wang, F., et al. 2023, *ApJ*, 956, 52, doi: [10.3847/1538-4357/acf12d](https://doi.org/10.3847/1538-4357/acf12d)
- Van Rossum, G., & Drake, F. L. 2009, *Python 3 Reference Manual* (Scotts Valley, CA: CreateSpace)
- Virtanen, P., Gommers, R., Oliphant, T. E., et al. 2020, *Nature Methods*, 17, 261, doi: [10.1038/s41592-019-0686-2](https://doi.org/10.1038/s41592-019-0686-2)
- West, A. A., Hawley, S. L., Walkowicz, L. M., et al. 2004, *AJ*, 128, 426, doi: [10.1086/421364](https://doi.org/10.1086/421364)